ANGLE-OF-ATTACK EFFECTS ON FLOWFIELD CHARACTERISTICS OF FLAT-NOSE LEADING EDGES IN HYPERSONIC FLOW

Wilson F. N. Santos
National Institute for Space Research
Combustion and Propulsion Laboratory
12630-000 Cachoeira Paulista, SP, Brazil
wilson@lcp.inpe.br

Abstract. *This work describes a computational investigation on rarefied hypersonic flow past flat-nose leading edges at incidence. Positive angle-of-attack effects on the flowfield structure have been investigated by employing the Direct Simulation Monte Carlo (DSMC) method. Effects are investigated of variation in angle of attack and frontal-face thickness of the leading edges in terms of the primary properties. Some significant differences between sharp and blunt leading edges were noted on the flowfield structure. It was found that the angle-of-attack variations have different influence on velocity, density, pressure and temperature along the stagnation streamline ahead of the leading edges as well as on the profiles adjacent to the body surface. The analysis showed that positive angle of attack causes the expected asymmetry in the flow patterns as the stagnation point moves from the symmetry axis to the windward side of the leading edges. Interesting features observed in the properties profiles showed that small leading edge thickness, compared to the freestream mean free path, still has important effects on high Mach number leading edge flows.*

Keywords*: Hypersonic Flow, Rarefied Flow, DSMC, Blunt Leading Edge, Angle-of-attack.*

1. INTRODUCTION

Projects about future hypersonic transport vehicles have led to renewed interest in the waverider concept. Waveriders are either supersonic or hypersonic lifting configurations which are generated from a known flowfield. Inverse designing supersonic and hypersonic vehicles from known flowfield was first developed by Nonweiler (1959). Based on sharp leading edges, Nonweiler (1959) presented aerodynamic shapes with high lift-to-drag (L/D) ratio that avoid leakage from the high-pressure undersurface to the uppersurface. This concept may contribute to fuel efficiency and may raise the economic viability of civil hypersonic transport aircraft, providing interesting aerodynamic coefficient for a hypersonic vehicle.

It has long been known that vehicle intended for hypersonic flight must have blunt leading edges in order to avoid the high temperatures that would exist at sharp leading edges using conventional thermal protection systems. Nevertheless, if a high L/D ratio is sought, the need for blunt leading edges will limit what could otherwise be achieved. Blunt leading edge promotes shock wave standoff, therefore, making leading edge blunting a major concern in the design and prediction of flowfields over hypersonic waverider configurations.

In this context, flat-nose leading edges may provide the required bluntness for heat transfer concerns with reduced departures from ideal aerodynamic performance. This concept is based on work available in the literature (Reller, 1957) that pointed out a method of designing low heat transfer bodies. The method is devised on the premise that the rate of heat transfer to the nose will be low if the local velocity is low, while the rate of heat transfer to the afterbody will be low if the local density is low. A typical body that results from this design method consists of a flat nose followed by a highly curved, but for the most part slightly inclined, afterbody surface.

A great deal of works (Santos, 2003, 2004a, 2004b, 2005, 2006 and 2007) has been carried out recently on flat-nose form representing blunt geometries. The major interest in these works has gone into considering the flat-nose shape as possible candidate for blunting geometries of hypersonic leading edges. Santos (2003) has investigated the sensitivity of the stagnation point heating and total drag to shape variations of such leading edges. The emphasis of the work was to compare flat-nose leading edges with round leading edges (circular cylinder) in order to determine which geometry would be better suited as a blunting profile in terms of stagnation point heating and total drag coefficient. The analysis showed that circular cylinder still provided smaller stagnation point heating than flat-nose leading edges under the range of conditions investigated. Nonetheless, flat-nose leading edges yielded lower total drag and much smaller shock standoff distance than the circular cylinder.

Santos (2006) extended further the analysis presented by Santos (2003) on flat-nose leading edges by performing a parametric study on these shapes with emphasis placed on the compressibility effects. The primary goal was to assess the sensitivity of the shock wave standoff distance, stagnation point heating and total drag due to changes on the freestream Mach number.

In continuation of the flat-nose body study, the purpose of the present account is to extend further the previous analysis on these leading-edge shapes by investigating the impact of the angle of attack on the flowfield structure. For positive angle of attack, important changes occur in the flowfield structure and in the aerodynamic surface quantities on blunt leading edges. This involves the modification of the flowfield properties and shock strength and, consequently,

some effects on aerodynamic forces acting on, and on heat transfer to the body surface. Moreover, the knowledge of these properties at zero-degree angle of attack is not sufficient to predict with certainty the flow characteristics over these shapes with incidence. Usually, for positive angle of attack, the incidence increase causes an asymmetry in the flow patterns as the stagnation point moves from the symmetry axis to the windward side of the body surface.

In an effort to obtain further insight into the nature of the flowfield structure of flat-nose leading edges under hypersonic transitional flow conditions, the essential characteristics of the angle of attack effect on the primary properties, such as velocity, density, pressure and temperature, will be examined for positive incidence with 5, 10, 15 and 20 degrees of incidence.

2. BODY SHAPE DEFINITION

The geometry of the leading edges considered in this work are the same as that presented in Santos (2003). The blunt shapes consist of a flat nose supplemented by an afterbody surface defined, in dimensionless form, by the following contour,

$$\bar{x} = \int_{\bar{y}=1}^{\bar{y}=\bar{y}_{\max}} \sqrt{\bar{y}^k - 1} \, d\bar{y} \qquad \text{where } \bar{x} = x/y_{nose} \text{ and } \bar{y} = y/y_{nose} \qquad (1)$$

The flat-nose shapes are modeled by assuming a sharp leading edge of half angle θ with a circular cylinder of radius R inscribed tangent to the wedge. The flat-nose shapes, inscribed between the wedge and the cylinder, are also tangent to them at the same common point where they have the same slope angle. The circular cylinder diameter provides a reference for the amount of blunting desired on the leading edges. It was assumed a leading edge half angle of 10 degrees, a circular cylinder diameter of 10^{-2}m and flat-nose thickness t/λ_∞ of 0.01, 0.1 and 1, where $t = 2y_{nose}$ and λ_∞ is the freestream mean free path. Figure 1(a) illustrates this construction for the set of shapes investigated. From geometric considerations, the exponent k in Eq. (1) is obtained by matching slope on the wedge, circular cylinder and on the body shapes at the tangency point. For dimensionless thickness t/λ_∞ of 0.01, 0.1 and 1, the exponent k corresponds to 0.501, 0.746 and 1.465, respectively. It was assumed that the leading edges are infinitely long but only the length L is considered, since the wake region behind the leading edges is not of interest in this investigation.
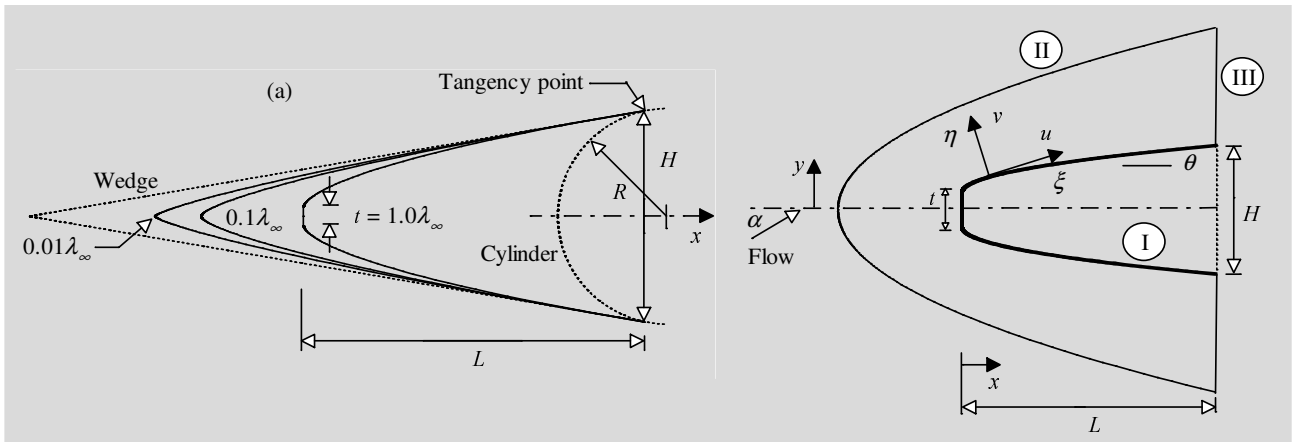

Figure 1: Drawing illustrating (a) the leading edge shapes and (b) the computational domain.

3. COMPUTATIONAL METHOD AND PROCEDURE

The Direct Simulation Monte Carlo (DSMC) method (Bird, 1994) is a computational technique for modeling complex transitional flows of engineering interest. The DSMC method model a gas flow by using a computer to track the trajectory of simulated particles, where each simulated particle represents a fixed number of real gas particles. The direct simulation of the physical processes is in contrast with computation fluid dynamics (CFD) method that is applied to the mathematical equations that model the physical processes.

The uncoupling of the molecular motion and collisions over small time steps and the division of the flowfield into small cells are the key computational assumptions associated with the DSMC method. The time step should be much less than the mean collision time (Alexander et al., 1998, Alexander et al., 2000) and a typical cell dimension should be much less than the local mean free path (Garcia and Wagner, 2000, and Hadjiconstantinou, 2000). The cell dimension should also be small compared with the distance over which there is a significant change in the flow properties. The DSMC method uses the cell system only for the sampling of the macroscopic properties and for the selection of possible

collision partner.

Molecular collisions are simulated with the Variable Hard Sphere (VHS) molecular model (Bird, 1981) and the no time counter (NTC) collision sampling technique (Bird, 1989). Energy exchange between kinetic and internal modes is controlled by the Borgnakke-Larsen statistical model (Borgnakke and Larsen, 1975). For the present account, the simulations are performed using nonreacting gas models, consisting of 76.3% of N_2 and 23.7% of O_2, while considering energy exchange between translational, rotational and vibrational modes. Relaxation collision numbers of 5 and 50 were used for the calculations of rotation and vibration, respectively.

The computational domain used for the calculation is adequate for capturing the major flow phenomena about the leading edges. A schematic view of the computational domain is depicted in Figure 1(b). Side I is defined by the body surface. Reflection with complete surface accommodation is the condition applied to this side. Side II is the freestream side through which simulated molecules enter and exit. Finally, the flow at the downstream outflow boundary, side III, is predominantly supersonic and vacuum condition is specified (Bird, 1994). At this boundary, simulated molecules can only exit.

The relevant freestream and flow conditions used in the present calculations are those given by Santos (2003) and summarized in Tabs. 1 and 2, respectively. The freestream velocity V_∞, assumed to be constant at 3.56 km/s, corresponds to freestream Mach number M_∞ of 12. The translational and vibrational temperatures in the freestream are in equilibrium at 220 K, and the leading edge surface has a constant temperature T_w of 880 K for all cases considered.

Table 1: Freestream Conditions

Temperature T_∞ (K)	Pressure p_∞ (N/m^2)	Density ρ_∞ (kg/m^3)	Number density n_∞ (m^{-3})	Viscosity μ_∞ (Ns/m^2)	Mean free path λ_∞ (m)	Velocity V_∞ (m/s)
220.0	5.582	8.753 x 10^{-5}	1.8209 x 10^{21}	1.455 x 10^{-5}	9.03 x 10^{-4}	3560

Table 2: Gas Properties

	Mole fraction X	Molecular mass m (kg)	Molecular diameter d (m)	Viscosity index ω
O_2	0.237	5.312 x 10^{-26}	4.01 x 10^{-10}	0.77
N_2	0.763	4.65 x 10^{-26}	4.11 x 10^{-10}	0.74

The overall Knudsen number Kn_t, defined as the ratio of the freestream mean free path λ_∞ to the leading edge thickness t, corresponds to 1, 10 and 100 for frontal-face thickness t/λ_∞ of 1, 0.1 and 0.01, respectively. The Reynolds number Re_t covers the range from 0.193 to 19.3, based on conditions in the undisturbed stream with frontal-face thickness t as the characteristic length.

In order to simulate the angle-of-attack effect, the DSMC calculations were performed independently for five distinct numerical values of α, i.e., 0, 5, 10, 15 and 20 degrees. It is important to mention that α equal to 0 represents the case investigated previously (Santos, 2003).

4. COMPUTATIONAL RESULTS AND DISCUSSION

The purpose of this section is to discuss and to compare differences in the flowfield properties due to variations on the angle of attack and on the leading-edge shape. Results will be illustrated by a series of profile plots of velocity, density, pressure and temperature.

4.1. Velocity Profiles

Variations of the tangential velocity u along the leeward and windward body surfaces are depicted in Figs. 2 and 3, respectively, as a function of the angle of attack α for the $Kn_t = 10$ case. In these figures, the velocity ratio stands for the tangential velocity u normalized by the freestream velocity V_∞, and the dimensionless height is the distance normal to the body surface along η-direction (see Fig. 1(b)), normalized by the freestream mean free path λ_∞. In an effort to emphasize points of interest, this set of plots presents data for three stations along the afterbody surface corresponding to the body slope angle of 80, 40 and 20 degrees. As a basis of comparison, for the $Kn_t = 10$ case, the body slope angle of 80, 40 and 20 degrees correspond to arc length s/λ_∞ of approximately 0.05, 0.2 and 1.6, respectively.

Of great significance in this set of figures is the slip velocity. It is seen that slip velocity increases on the leeward side and decreases on the windward side of the leading edge with increasing the angle of attack. A similar behavior is observed for the other two thickness Knudsen number cases investigated, Kn_t of 100 and 1. It is important to mention that as $\eta \rightarrow \infty$, $u \rightarrow u_\infty$ ($\equiv V_\infty cos\theta cos\alpha$). In this sense, it is clearly seen in Figs. 2 and 3 that the tangential velocity

reaches the freestream limit value u_∞ around 3, 4 and $6\lambda_\infty$ above the surface for stations corresponding to body slope angle of 80, 40 and 20 degrees, respectively. In contrast, for $Kn_t = 1$ case, the tangential velocity (not shown) reaches the limit value around 6, 7 and $10\lambda_\infty$ above the surface for the same stations. This is explained by the fact that the leading edge changes from sharp to blunt one as the frontal-face thickness increases from t/λ_∞ of 0.01 ($Kn_t = 100$) to 1 ($Kn_t = 1$). Sharp leading edge is more streamlined than blunt leading edge. Consequently, the flowfield adjacent to the body surface is less affected by the body shape.

Still referring to Figs. 2 and 3, it is encouraging to observe that significant differences in the velocity profiles along the leeward and windward sides occur adjacent to the body surface. In addition, as indeed is clear from these figures, there is no backflow on the leeward side of the body surface, even though for the $\alpha = 20°$ case.
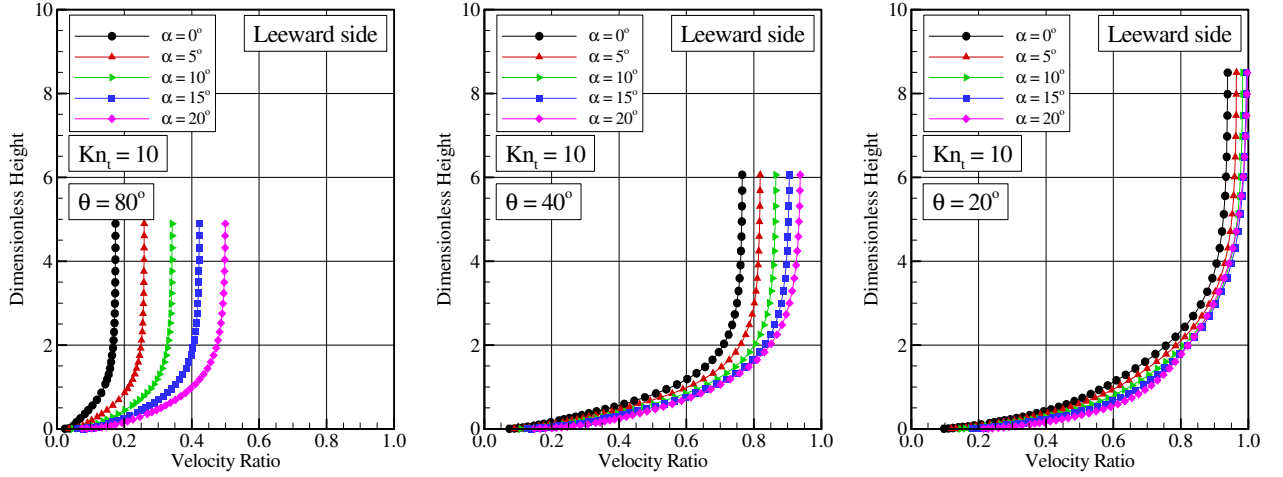

Figure 2: Tangential velocity (u/V_∞) profiles along the body leeward side as a function of the angle of attack for Kn_t of 10 at afterbody stations corresponding to body slope angle of (a) 80, (b) 40 and (c) 20 degrees.
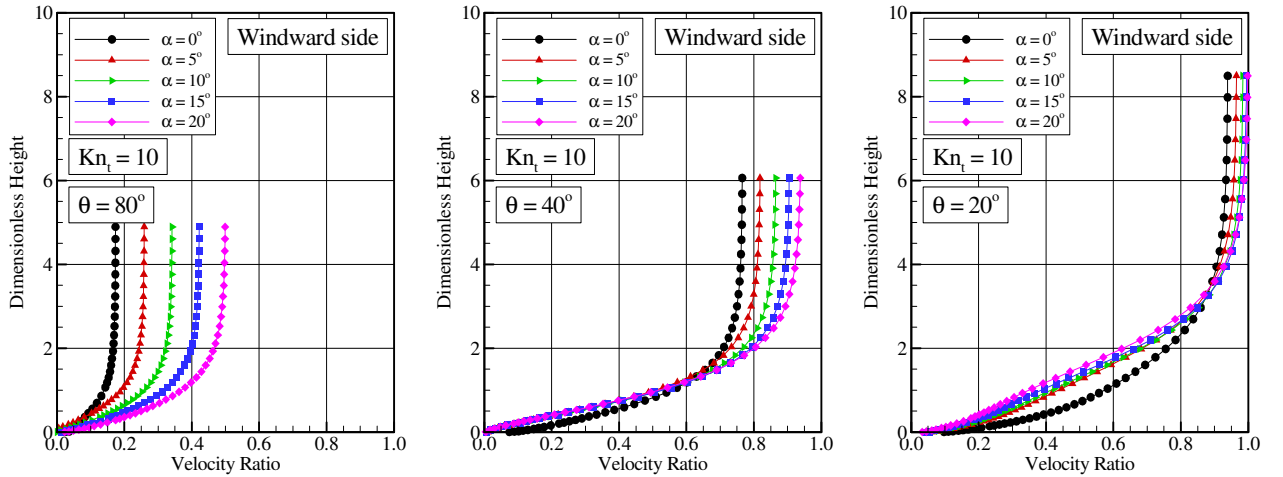

Figure 3: Tangential velocity (u/V_∞) profiles along the body windward side as a function of the angle of attack for Kn_t of 10 at afterbody stations corresponding to body slope angle of (a) 80, (b) 40 and (c) 20 degrees.

4.2. Density Profiles

Density profiles along the symmetry axis upstream the leading edges are illustrated as a function of the angle of attack α in Figs. 4(a-c) for thickness Knudsen number Kn_t of 100, 10 and 1, respectively. In this group of figures, density ratio represents the density ρ normalized by the freestream density ρ_∞, and the dimensionless length is the length x normalized by the freestream mean free path λ_∞. Also, the flow is from the left-hand side to the right-hand side. According to this set of plots, it is observed that there is a continuous rise in density from the freestream to the nose of the leading edges, rising to well above the continuum inviscid limit for the cases investigated. As a point of reference, the Rankine-Hugoniot relations give a postshock density that corresponds to the ratio $\rho/\rho_\infty = 5.8$ for freestream Mach number of 12.
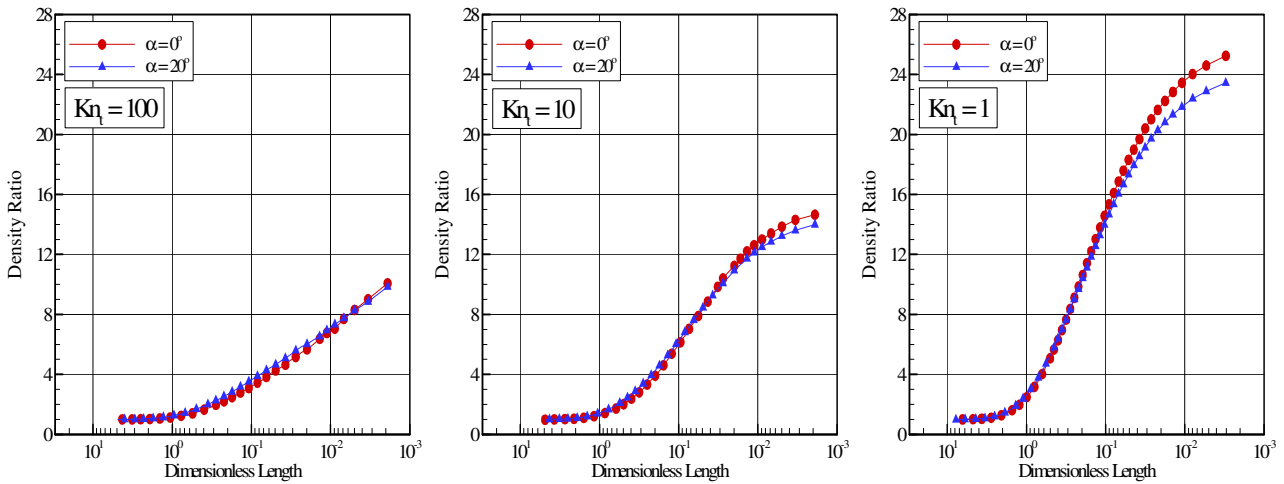
Figure 4: Density ratio (ρ/ρ_∞) profiles along the symmetry axis as a function of the angle of attack for thickness Knudsen number Kn_t of (a) 100, (b) 10 and (c) 1.
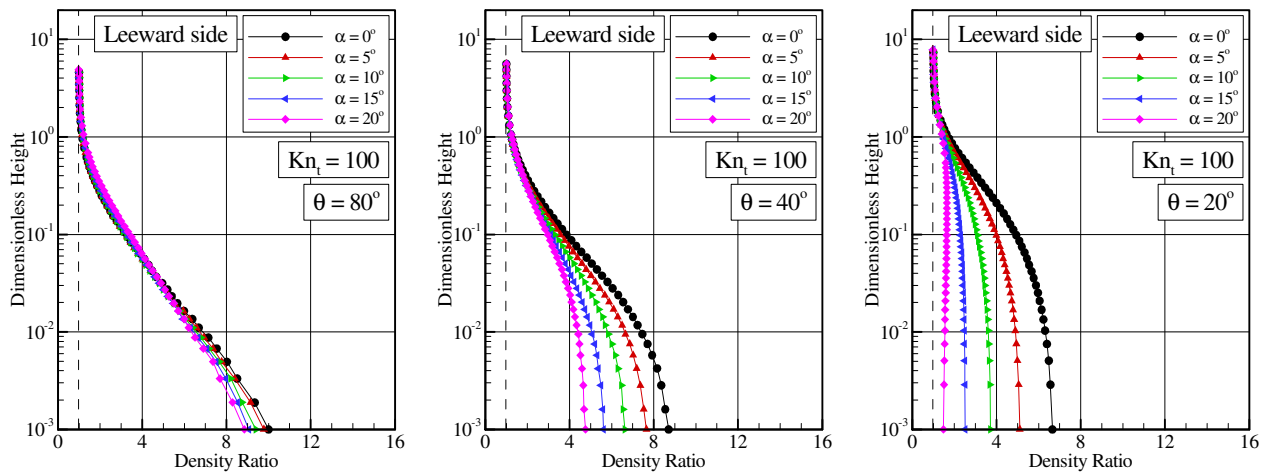

Figure 5: Density ratio (ρ/ρ_∞) profiles along the body leeward side as a function of the angle of attack for Kn_t of 100 at afterbody stations corresponding to body slope angle of (a) 80, (b) 40 and (c) 20 degrees.
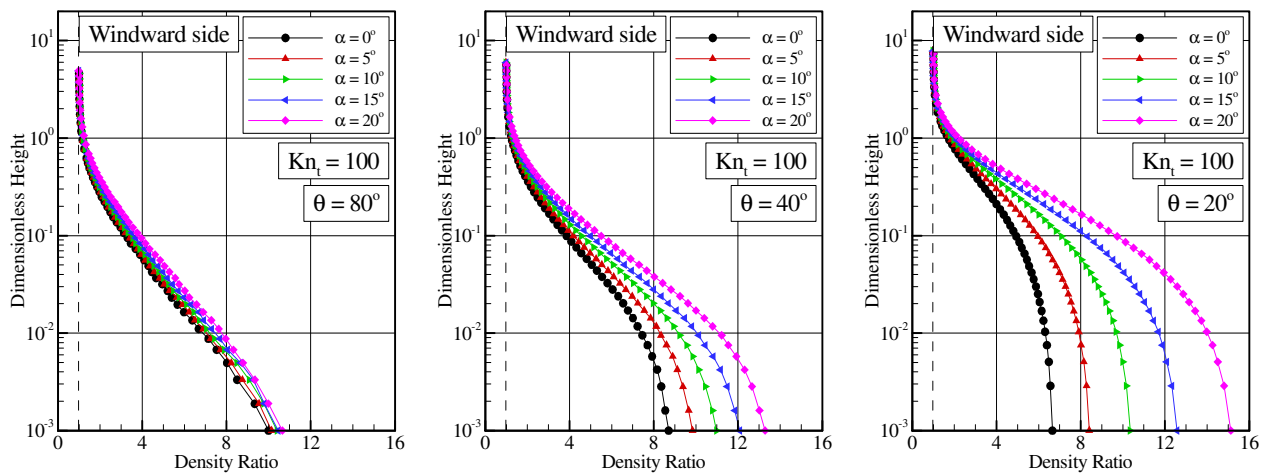

Figure 6: Density ratio (ρ/ρ_∞) profiles along the body windward side as a function of the angle of attack for Kn_t of 100 at afterbody stations corresponding to body slope angle of (a) 80, (b) 40 and (c) 20 degrees.

It can be also recognized from Figs. 4(a-c) that density raises gradually as the flow approaches the nose of the leading edge, indicating the diffuse nature of the shock wave, a characteristic of highly rarefied flows. Near the origin point ($\eta/\lambda_\infty \approx 0$), a substantial density increase occurs for the cases shown. This density increase is a characteristic of a cold-wall entry flow. In typical entry flow, the body surface temperature is low compared to the stagnation temperature. This leads to a steep density gradient near the body surface. For the present simulations, the ratio of wall temperature to stagnation temperature is 0.13, which corresponds to a cold-wall flow. In addition, at incidence, no significant changes are observed in the density profiles along the symmetry line, except for the $Kn_t = 1$ case where density ratio decreases from around 26 to 23 as the angle of attack increases from 0 to 20 degrees.

Density profiles along the leeward and windward body surfaces are demonstrated in Figs. 5 and 6, respectively, for Kn_t of 100, parameterized by the angle of attack α. This set of plots displays selected profiles for three afterbody stations, body slope angles of 80, 40 and 20 degrees, along the leeward and windward surfaces, measured from the shoulders of the leading edges. By examining the density profiles depicted in these figures, it is observed that positive incidence produces the expected behavior on both surfaces in that density decreases on the leeward side and increases on the windward side. On the leeward side, density decreases below the density for the zero-incidence case as a result of the flow expansion along the leeward surface. In contrast, on the windward side, density rises above that for the zero-incidence case as a consequence of the flow compression along the windward surface. Particular attention should be paid to the density ratio profiles for angle of attack α of 20 degrees, as shown in Fig. 5(c). For this case, the attained density on the leeward side approaches the freestream density. Nevertheless, on the windward side, Fig. 6, compression combined with the relatively cool wall produces density around one order of magnitude larger than the freestream density. It is important to mention that a similar behavior for density profiles is observed for the other leading edges cases, i.e., thickness Knudsen number Kn_t of 10 and 1.

In what follows, density ratio contours are depicted in Figs. 7(a-c) for leading edges corresponding to Kn_t of 100, 10 and 1, respectively, and angle of attack of 20 degrees. In this set of diagrams, X and Y stand for the length x and height y normalized by the freestream mean free path λ_∞.
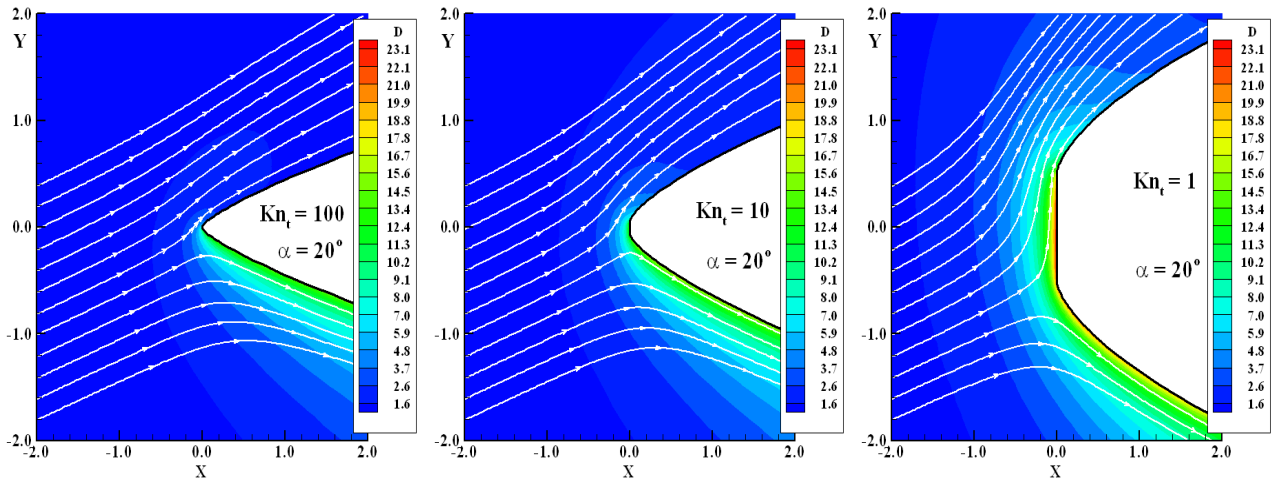

Figure 7: Density ratio (ρ/ρ_∞) contours at the vicinity of the leading edges defined by thickness Knudsen number Kn_t of (a) 100, (b) 10 and (c) 1, and angle of attack of 20 degrees.

Referring to Figs 7(a-c), it is observed that the major changes in density occur in a thin region close to the body surface. At zero-degree angle of incidence (see Fig. 4), the pick in density occurs at the stagnation point, and the high value is attained for the bluntest leading edge investigated, for the $Kn_t = 1$ case. As the incidence increases, density increases along the windward side and diminishes faster along the leeward side, since the flow is found to accelerate more quickly from the stagnation point downstream along the leeward side of the leading edges.

Also of great significance is the disturbance domain upstream the frontal face of the leading edges. The upstream disturbance caused in the density profiles is more pronounced for the bluntest leading edge investigated, i.e., for the $Kn_t = 1$ case. A similar behavior is observed in the velocity profiles.

4.3. Pressure Profiles

The large amount of kinetic energy present in a hypersonic freestream is converted by molecular collisions into high thermal energy surrounding the body and by flow work into increased pressure. In this respect, the stagnation line is a zone of strong compression, where pressure increases from the freestream to the stagnation point due to the shock wave that forms ahead of the leading edges.

Distributions of pressure ratio profiles along the symmetry axis are shown as a function of the angle of attack α in Figs. 8(a-c) for Kn_t of 100, 10 and 1, respectively. In this set of diagrams, pressure ratio is the pressure p normalized by the freestream pressure p_∞. As can be seen, there is a continuous rise in pressure from the freestream up to the frontal face of the leading edges. Near the origin point, stagnation point for the zero-incidence case, a substantial pressure increase occurs with increasing the leading edge thickness t. In addition, as indeed is clear from these figures, the general shape of the pressure profiles is preserved along the symmetry line when the angle of attack is increased from 0 to 20 degrees. It is also seen that pressure decreases at the vicinity of the frontal face with increasing the angle of attack.
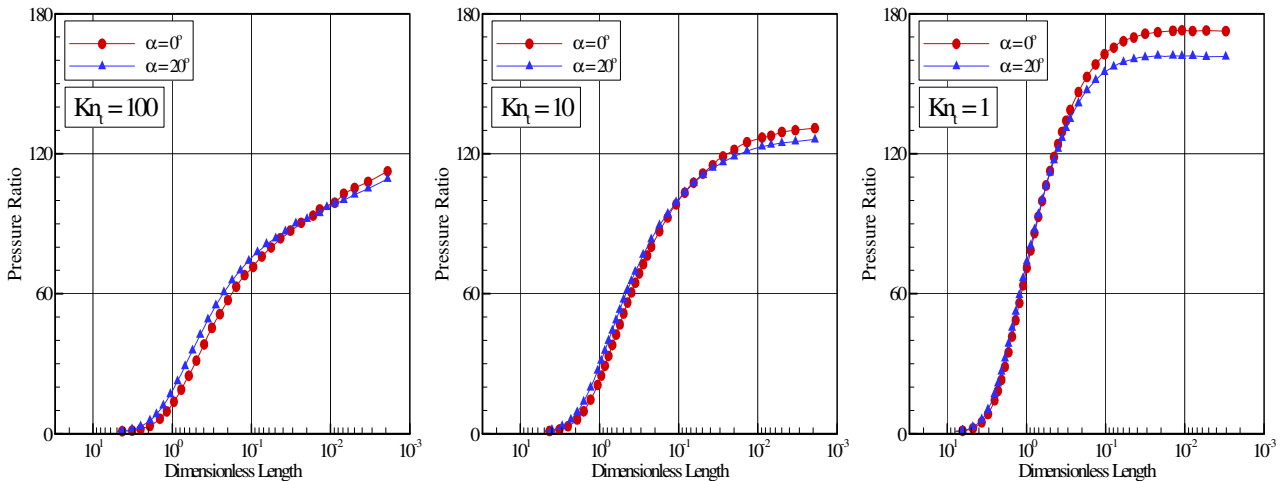

Figure 8: Pressure ratio (p/p_∞) profiles along the symmetry axis as a function of the angle of attack for Knudsen number Kn_t of (a) 100, (b) 10 and (c) 1.

Local pressure ratio profiles for three stations located on the leeward and windward body surfaces are displayed in Figs. 9 and 10, respectively, for the $Kn_t = 10$ case. It is noticed from these profiles that pressure is dramatically affected by the angle-of-attack rise. Similar to density, pressure decreases on the leeward side and it increases on the windward side of the body surface. At the station $\theta = 20$ degrees, pressure reduces from 60 to around 20 times the freestream pressure value for an incidence of 20 degrees. In contrast, for the same position on the windward side, the pressure rise is in excess of almost two orders of magnitude in comparison to the freestream pressure value for the same incidence.

In what follows, a critical assessment of the flowfield is provided by Figs. 11(a-c), which consider a magnification of the pressure ratio, p/p_∞ at the vicinity of the leading-edge nose for Kn_t of 100, 10 and 1, respectively, with angle of attack of 20 degrees. This group of figures confirms that the stagnation region is a zone of strong compression. Moreover, the extent of the upstream flowfield disturbance for pressure is significantly different from that presented by density. It is also seen that the upstream domain of influence for pressure is higher than that for density and lower than that presented for temperature, as will be seen subsequently.
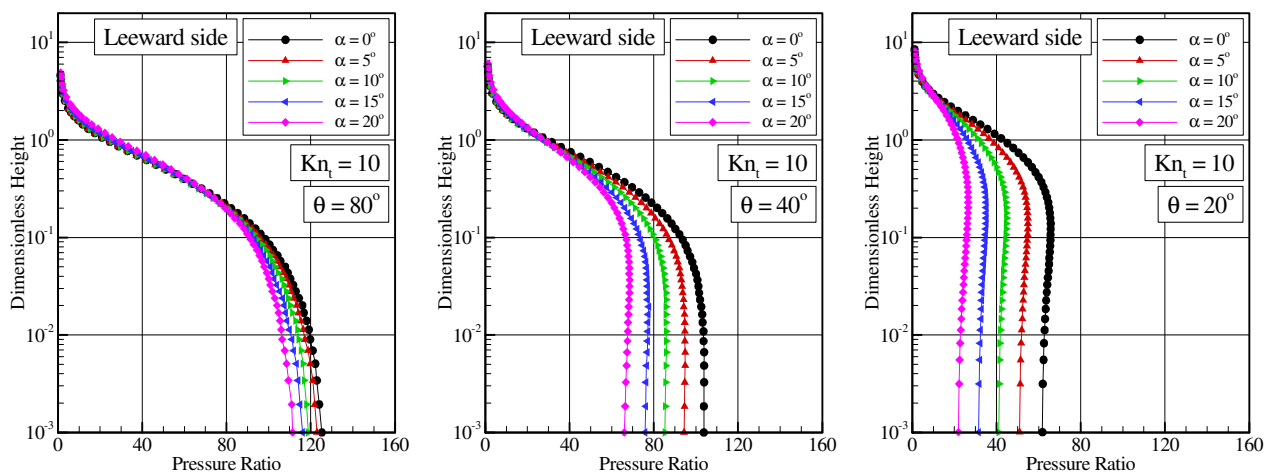

Figure 9: Pressure ratio (p/p_∞) profiles along the body leeward side as a function of the angle of attack for Kn_t of 10 at afterbody stations corresponding to body slope angle of (a) 80, (b) 40 and (c) 20 degrees.
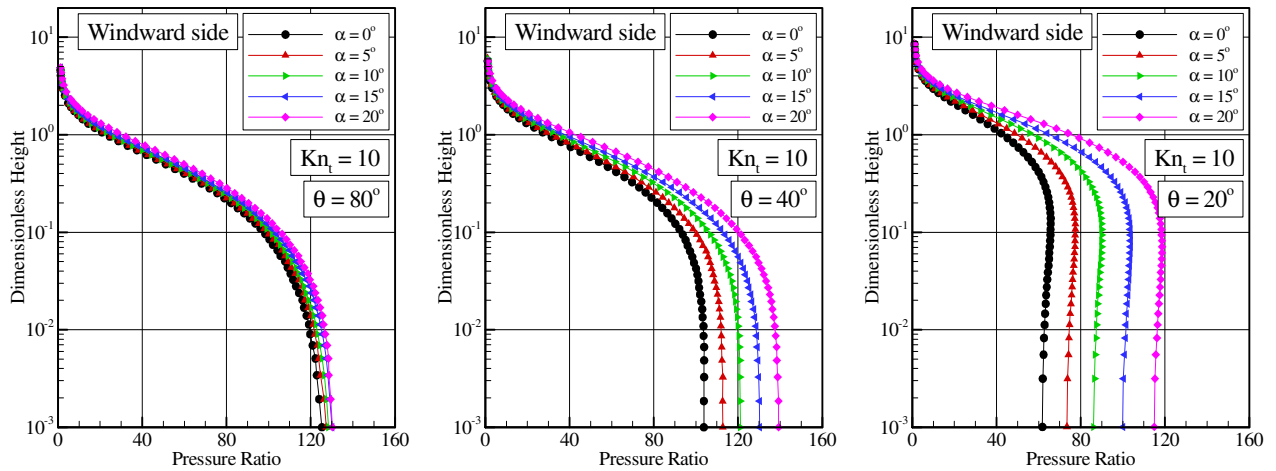
Figure 10: Pressure ratio (p/p_∞) profiles along the body windward side as a function of the angle of attack for Kn_t of 10 at afterbody stations corresponding to body slope angle of (a) 80, (b) 40 and (c) 20 degrees.
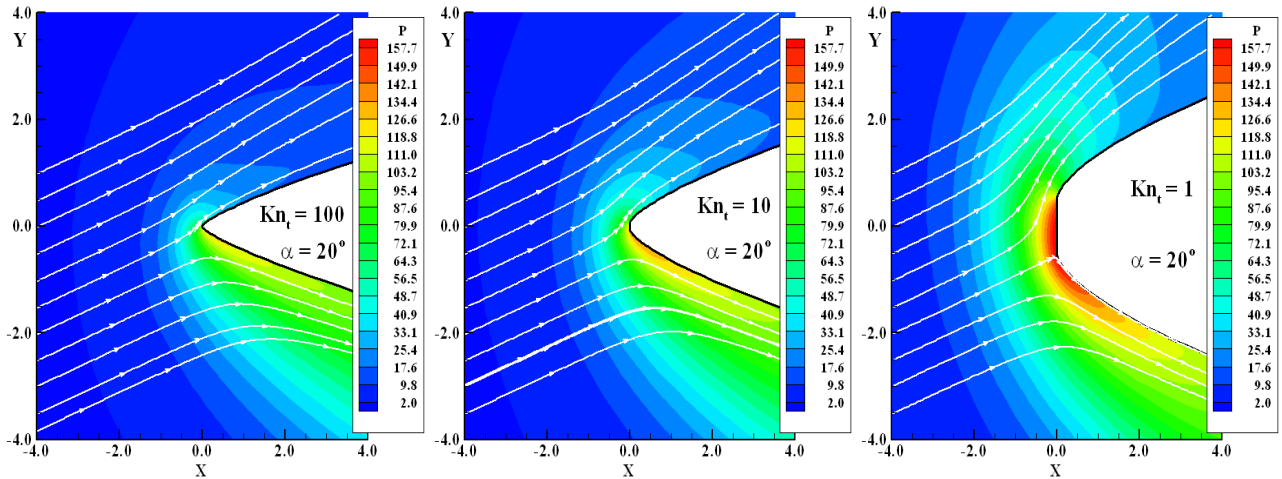

Figure 11: Pressure ratio (p/p_∞) contours at the vicinity of the leading edges defined by thickness Knudsen number Kn_t of (a) 100, (b) 10 and (c) 1, and angle of attack of 20 degrees.

4.4. Temperature Profiles

The strong shock wave that forms ahead of a blunt leading edge at hypersonic flow converts part of the kinetic energy of the freestream air molecules into thermal energy. This thermal energy downstream of the shock wave is partitioned into increasing the translational kinetic energy of the air molecules, and into exciting other molecular energy states such as rotation and vibration.

Temperature ratio profiles along the symmetry axis upstream the leading edges are displayed in Figs. 12(a-c) for Kn_t of 100, 10 and 1, respectively. In this set of diagrams, temperature ratio stands for the translational temperature T_T, rotational temperature T_R, vibrational temperature T_V or overall temperature T_{OV} normalized by the freestream temperature T_∞. Also, filled and empty symbols correspond to temperature distributions for angle of attack of 0 and 20 degrees, respectively. Again, flow is from left-hand side to right-hand side. It is apparent from these figures that thermodynamic nonequilibrium occurs throughout the shock layer, as shown by the lack of equilibrium of the translational and internal kinetic temperatures. Thermal nonequilibrium occurs when the temperatures associated with translational, rotational, and vibrational modes of a polyatomic gas are different. In such a context, it proves convenient to define the overall kinetic temperature, obtained for a nonequilibrium gas as the weighted mean of the translational and internal temperatures. The overall kinetic temperature is equivalent to the thermodynamic temperature only in thermal equilibrium conditions.

Still referring to Figs. 12(a-c), it is clearly seen that the angle-of-attack impact is more significant in the temperature profiles for the sharp and aerodynamically sharp leading edges, i.e., Kn_t of 100 and 10. Conversely, no appreciable changes are observed for the bluntest leading edge investigated, Kn_t of 1.
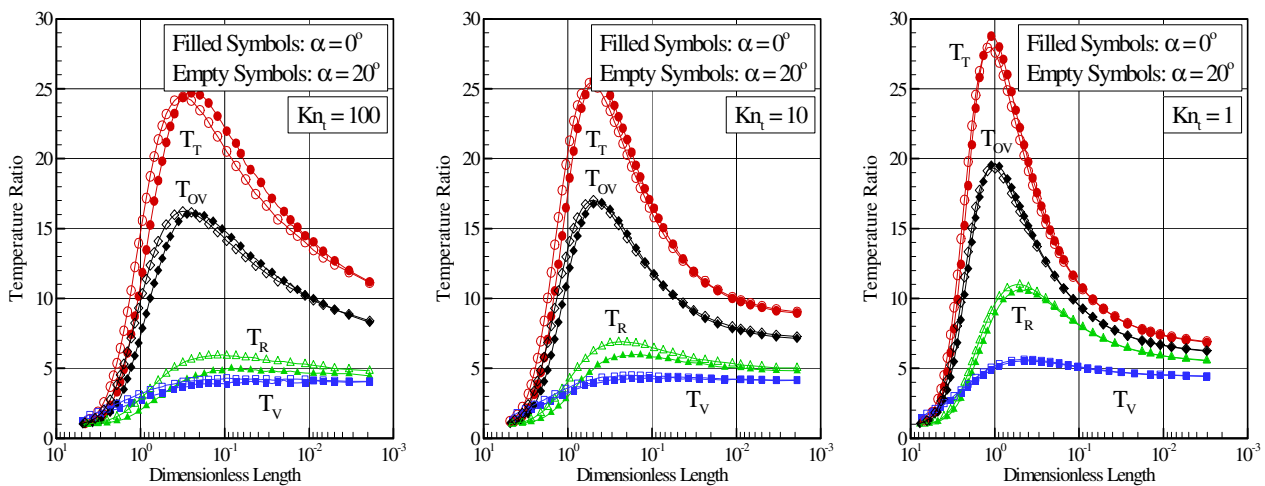
Figure 12: Temperature ratio (T/T_∞) profiles along the symmetry axis as a function of the angle of attack for Knudsen number Kn_t of (a) 100, (b) 10 and (c) 1.

In the following, it becomes instructive to illustrate the effect on the overall kinetic temperature along the leading edge surfaces due to the changes on the angle of attack α. In this fashion, the overall kinetic temperature variations is taken normal to the body surface at afterbody stations corresponding to the body slope angle of 80, 40 and 20 degrees, measured from the frontal-face/afterbody junction of the leading edges. Figures 13 and 14 depict profiles of overall kinetic temperature ratio for Kn_t of 1 at the considered positions along the leeward and windward body surfaces, respectively. In this set of figures, temperature ratio stands for the overall kinetic temperature T_{OV} normalized by the freestream temperature T_∞.

According to Figs. 13 and 14, it is clearly noticed that, compared to the overall kinetic temperature for zero-incidence case, the overall kinetic temperature increases along the leeward side and decreases along the windward side of the body surface inside a small region adjacent to the body surface. This is in contrast to the density behavior presented previously in that density decreases in the leeward side and increases in the windward side of the leading edges. It should be mentioned in this context that the ideal gas equation of state does not apply to a thermal nonequilibrium situation.

Of particular interest in the analysis is also the behavior of the overall kinetic temperature in comparison to the wall temperature T_w. According to the prescribed conditions, the wall temperature was set four times the freestream temperature, i.e., $T_w/T_\infty = 4$. Therefore, the ratio of the overall kinetic temperature to the wall temperature, T_{OV}/T_w, is given by $0.25(T_{OV}/T_\infty)$. As a result, with this in mind, it is observed from Figs. 13 and 14 that the overall kinetic temperature reaches a value on both leeward and windward surfaces that is above the wall temperature, resulting in a temperature jump as defined in continuum formulation. The temperature jump behavior observed is similar to the slip velocity one (see Figs. 2 and 3) in that both temperature jump and slip velocity increase on the leeward side and decrease on the windward side of the leading edges due to an angle-of-attack rise.

According to Figs. 13 and 14, it is clearly noticed that the downstream evolution of the flow on both leeward and windward sides displays a smearing tendency of the shock wave due to the displacement of the maximum value for the overall kinetic temperature. Also, it may be recognized from the overall kinetic temperature distribution in Figs. 13 and 14 that significant changes in the overall kinetic temperature profiles occur within a thin layer adjacent to the body surface for the range of incidence angle investigated.

In order to bring out important features of the angle-of-attack effects, particular attention is paid to the overall kinetic temperature at the vicinity of the leading edges. In this scenario, overall kinetic temperature contours, normalized by the freestream temperature T_∞, are plotted in Figs. 15(a-c) for leading edges corresponding to Kn_t of 100, 10 and 1, respectively. This set of plots clearly illustrates the asymmetry in the flow patterns, produced by an increase in the angle of attack, as the stagnation point moves from the axis of symmetry to a station on the windward side of the body surface. As the incidence increases, the peaks in the overall kinetic temperature ahead of the body follows the location of the stagnation streamline and move from the axis of the body toward the windward side of the body. At the same time, the expansion on the leeward side extends further out into the flow. Substantial differences in the overall kinetic temperature are observed as the frontal-face thickness changes from 0.01 to 1, i.e., as the thickness Knudsen number Kn_t is reduced from 100 to 1. For instance, the overall kinetic temperature core is located roughly on the nose of the leading edge for the $Kn_t = 100$ case. Nevertheless, it is about one freestream mean free path ahead of the stagnation point for the $Kn_t = 1$ case, showing that the upstream disturbance becomes more pronounced as the leading edge becomes blunter.
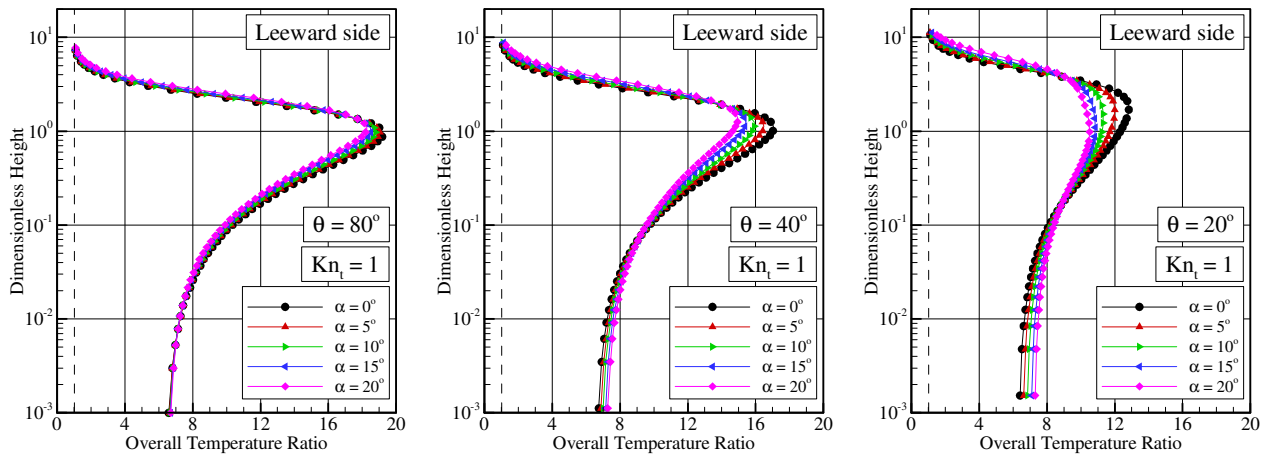
Figure 13: Overall temperature ratio (T_{OV}/T_∞) profiles along the body leeward side as a function of the angle of attack for Kn_t of 1 at afterbody stations corresponding to body slope angle of (a) 80, (b) 40 and (c) 20 degrees.
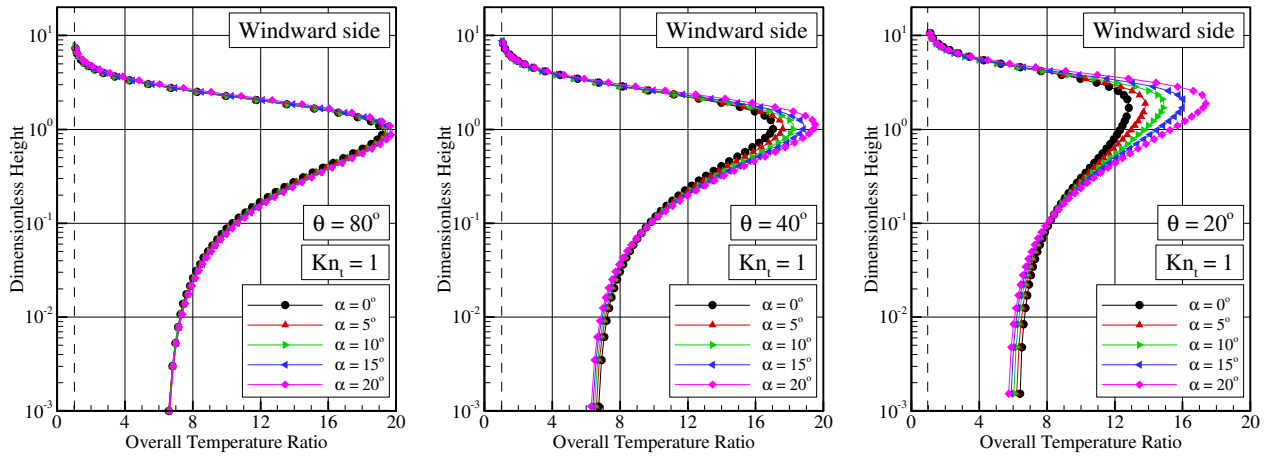

Figure 14: Overall temperature ratio (T_{OV}/T_∞) profiles along the body windward side as a function of the angle of attack for Kn_t of 1 at afterbody stations corresponding to body slope angle of (a) 80, (b) 40 and (c) 20 degrees.
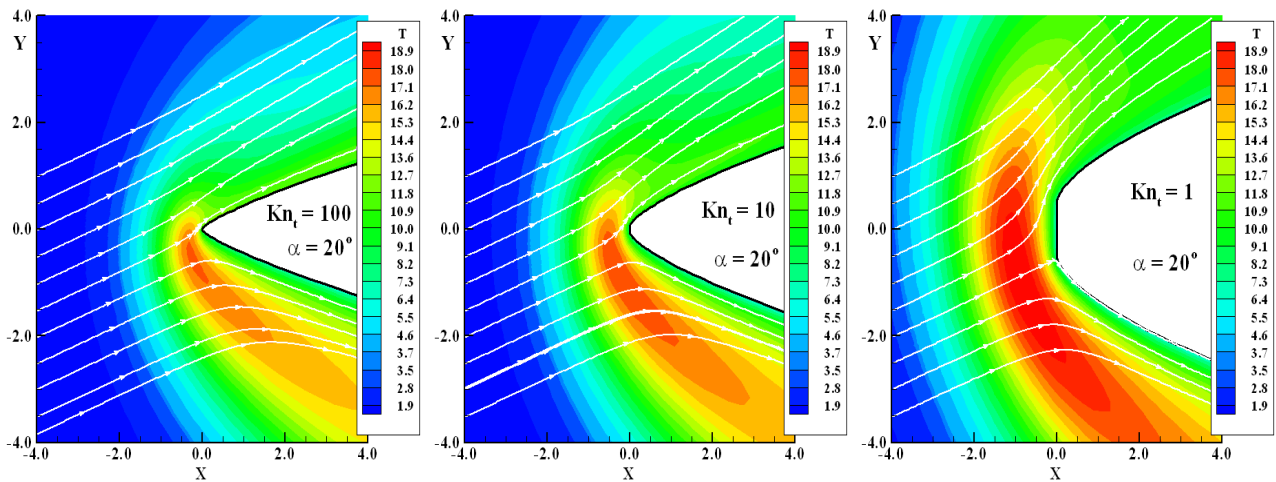

Figure 15: Overall temperature ratio (T_{OV}/T_∞) contours at the vicinity of the leading edges defined by thickness Knudsen number Kn_t of (a) 100, (b) 10 and (c) 1, and angle of attack of 20 degrees.

5. CONCLUDING REMARKS

This study applies the Direct Simulation Monte Carlo method to investigate rarefied gas over flat-faced leading edges. Effects of the angle of attack on the primary properties such as velocity, density, pressure and temperature are investigated. The angle of attack varied from 0 to 20 degrees, and the thickness of the frontal surface considered in this study covers hypersonic flow from the transitional flow regime to the free molecular flow.

It was found that changes on the angle of attack as well as on the leading-edge shape disturbed the flowfield around the leading edges. The domain of influence increased by increasing the frontal-face thickness, as the leading edge changed from sharp to blunt one. Moreover, the extent of the flowfield disturbance on both leeward and windward sides of the body surfaces due to the incidence was significantly different for each one of the primary flow properties. The analysis showed that the domain of influence for temperature is larger than that observed for pressure, density and velocity.

6. REFERENCES

Alexander, F. J., Garcia, A. L., and, Alder, B. J., 1998, "Cell Size Dependence of Transport Coefficient in Stochastic Particle Algorithms", Physics of Fluids, Vol. 10, No. 6, pp. 1540-1542.

Alexander, F. J., Garcia, A. L., and, Alder, B. J., 2000, "Erratum: Cell Size Dependence of Transport Coefficient is Stochastic Particle Algorithms", Physics of Fluids, Vol. 12, No. 3, pp. 731-731.

Bird, G. A., 1981, "Monte Carlo Simulation in an Engineering Context", Progress in Astronautics and Aeronautics: Rarefied gas Dynamics, Ed. Sam S. Fisher, Vol. 74, part I, AIAA New York, pp. 239-255.

Bird, G. A., 1989, "Perception of Numerical Method in Rarefied Gasdynamics", Rarefied gas Dynamics: Theoretical and Computational Techniques, Eds. E. P. Muntz, and D. P. Weaver and D. H. Capbell, Vol. 118, Progress in Astronautics and Aeronautics, AIAA, New York, pp. 374-395.

Bird, G. A., 1994, "Molecular Gas Dynamics and the Direct Simulation of Gas Flows", Oxford University Press, Oxford, England, UK.

Borgnakke, C. and Larsen, P. S., 1975, "Statistical Collision Model for Monte Carlo Simulation of Polyatomic Gas Mixture", Journal of Computational Physics, Vol. 18, No. 4, pp. 405-420.

Garcia, A. L., and, Wagner, W., 2000, "Time Step Truncation Error in Direct Simulation Monte Carlo", Physics of Fluids, Vol. 12, No. 10, 2000, pp. 2621-2633.

Hadjiconstantinou, N. G., 2000, "Analysis of Discretization in the Direct Simulation Monte Carlo", Physics of Fluids, Vol. 12, No. 10, pp. 2634-2638.

Nonweiler, T. R. F., 1959, "Aerodynamic Problems of Manned Space Vehicles", Journal of the Royal Aeronautical Society, Vol. 63, No. 589, pp. 521-528.

Reller Jr., J. O., 1957, "Heat Transfer to Blunt Nose Shapes with Laminar Boundary Layers at High Supersonic Speeds", NACA RM-A57FO3a.

Santos, W. F. N., 2003, "Aerodynamic Heating on Blunt Nose Shapes in Rarefied Hypersonic Flow", Proceedings of the 17th International Congress of Mechanical Engineering COBEM 2003, 10-14 Nov, São Paulo, SP, Brazil.

Santos, W. F. N., 2004a, "A Numerical Study of Drag and Heat Transfer to Blunt Nose Shapes in Rarefied Hypersonic Flow", Proceedings of the 24th International Congress of the Aeronautical Sciences, ICAS 2004, 29 Aug – 3 Sept, Yokohama, Japan.

Santos, W. F. N., 2004b, "Surface Temperature Effects in Low-Density Flow over Flat-Nose Bodies at Hypersonic Speed. Part I: Flowfield Structure", Proceedings of the 10th Brazilian Congress of Thermal Sciences and Engineering ENCIT 2004, 29 Nov – 3 Dec, Rio de Janeiro, RJ, Brazil.

Santos, W. F. N., 2005, "Gas-Surface Impact on Flowfield Structure of Low-Density Hypersonic Flow over Flat-Nose Bodies", Proceedings of the 18th International Congress of Mechanical Engineering COBEM 2005, 6-11 Nov, Ouro Preto, MG, Brazil.

Santos, W. F. N., 2006, "Compressibility Effect on Aerodynamic Heating and Drag of Hypersonic Flow over Flat-Nose Leading Edges", Proceedings of the 11th Brazilian Congress of Thermal Sciences and Engineering ENCIT 2006, 5 – 8 Dec, Curitiba, PR, Brazil.

Santos, W. F. N., 2007, "Simulation of Blunt Leading Edge Aerothermodynamics in Rarefied Hypersonic Flow". Journal of the Society of Mechanical Sciences and Engineering, Vol. 29, No. 2, pp. 123-135.